nature portfolio

https://doi.org/10.1038/s41586-022-05341-5

Supplementary information

Cumulative polarization in conductive interfacial ferroelectrics

In the format provided by the authors and unedited

Cumulative Polarization in Conductive Interfacial Ferroelectrics

Supplementary Information

Swarup Deb[1#], Wei Cao[2#], Noam Raab[1], Kenji Watanabe[3], Takashi Taniguchi[4], Moshe Goldstein[1], Leeor Kronik[5], Michael Urbakh[2], Oded Hod[2], Moshe Ben Shalom[1*]

Contents

S1. Device characterization 2
- a. Device detail 2
- b. Further details on AFM assessment 2
- c. Triangular Domain Formation 3
- d. 2D polarization calculation 4
- e. Cumulative polarization magnitude 4

S2. Finite Ferroelectric-like coupling of two active interfaces 5

S3. Doping and de-polarization measurements 5

S4. Calculation of multi-layered WSe_2 and MoS_2 polarization 7

S5. Calculation of doping-induced depolarization in WSe_2 and MoS_2 9

S6. Effect of polarization on the band-structure 15

List of Figures

Figure S1. Further device characterization. 3

Figure S2. Doping and depolarization measurements.. 7

Figure S3. Potential and charge density profiles of WSe_2 and MoS_2 bilayers. 8

Figure S4. Convergence tests.. 9

Figure S5. Potential and charge density profiles for WSe_2 and MoS_2 bilayer. 11

Figure S6. Convergence tests. 11

Figure S7. Effect of doping on the interlayer potential drop.. 12

Figure S8. Band structure and Fermi level variations with doping charge density.. 13

Figure S9. Comparison of different doping schemes.. 14

Figure S10. Effect of polarization on the band structure. 15

S1. Device characterization

a. Device detail

Device Name	**Electrode**	***h*-BN spacer thickness (nm)**
Dev 1: MoS_2	Au	6.3
Dev 2: WSe_2	Few layer graphene	12
Dev 3: WSe_2	Au	5.1

Table S1. Details of reported devices.

b. Further details on AFM assessment

Obtaining a reliable quantitative assessment of the absolute surface potential in KPFM measurements is challenging and requires delicate calibration processes[1–3], including the use of different tips, substrates, *h*-BN thicknesses, height of the tip above the surface, and amplitude/frequency (side-band) operation mode (see Ref. 4 of the main text). We note that the surface potential was found to be independent of the h-BN stack thickness in the range of 1-10 nm, as long as the dimensions of the domain were > 300x300 nm2. Hence, we focus our analysis on large domains, where the potential away from the domain wall saturates. Importantly, the analyses and conclusions in the present work rely on the relative change of the surface potential between two adjacent and oppositely polarized domains (see Fig. 1b), or on the relative change in the gate voltage (Fig. 3d), rather than on absolute values. The relative changes are considerably less prone to calibration uncertainties.

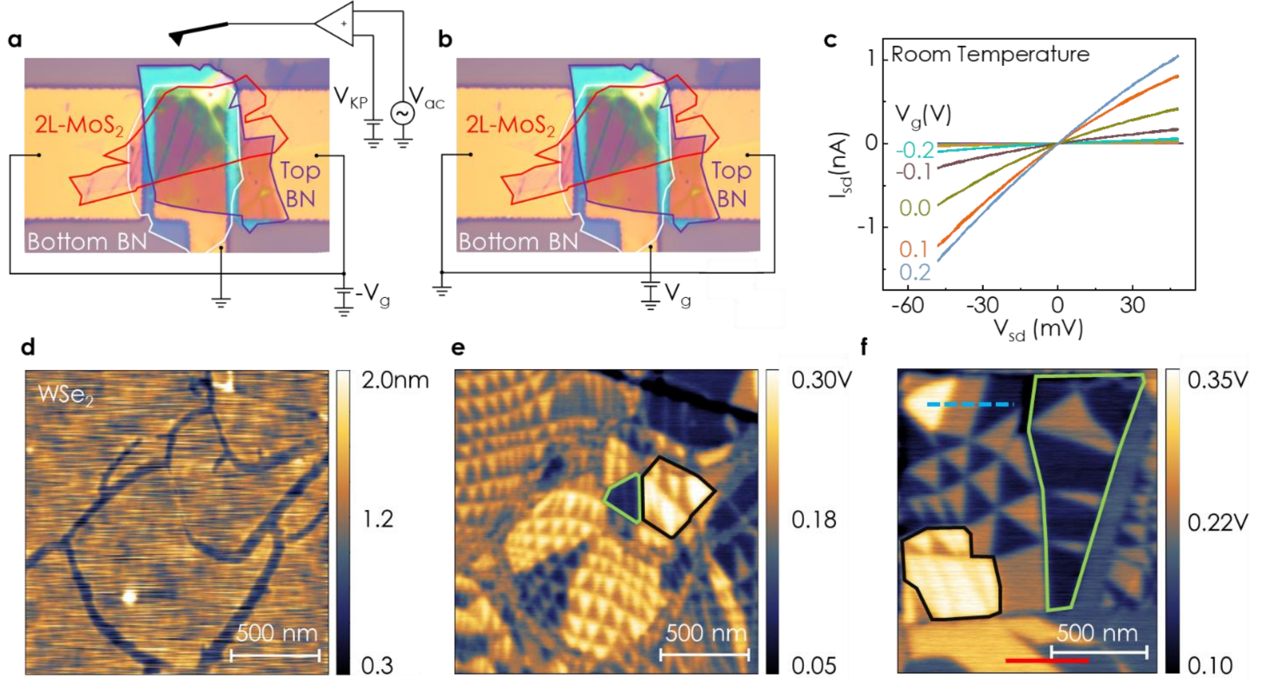

Figure S1. Further device characterization. (a,b) Optical microscope image of a typical device. Two circuit configurations of gating and KPFM measurement are illustrated. (**c**) The electric current along the MoS_2 bilayers is measured versus the source-drain bias (V_{sd}) and plotted for several fixed gate voltages (V_g) at room temperature. (**d,e**) Simultaneous measurement of topography and KPFM maps for a tri-layer WSe_2 structure (also shown in Fig.1 in the main text). The dark regions in the topography map indicate a crack in one of the layers, separating regions of trilayers with one and two active interfaces. (**e,f**) Examples of ferroelectric-like coupling between the two active interfaces in large-area domains. The ↑↓ (ABA, neutral color, 0.2V) domains cover a smaller area than the ↓↓ (CBA, dark, 0.02V) domains (circumscribed in green). The same is found for ↑↑ (ABC, bright, 0.3V) regions marked in black. The solid red and dashed blue lines in (f) mark the line cut position of the data shown in the main-text, Fig. 1b.

c. Triangular Domain Formation

The domain walls exhibit an intriguing geometrical structure that emerges due to the slight twist angle between the flakes and affects the entire atomically reconstructed triangular lattice. The shear boundary conditions of the artificial stacking experiments result in a shear deformation of precisely one planar interatomic spacing in each domain wall[4] (for WSe_2, each domain contributes a shear of $3.3/\sqrt{3}$ Å). In fact, for a given global twist angle, there is a fixed number of crossing points between domain walls that is determined by the moiré

superstructure topology. In our previous study (Ref. 4), we modeled the triangular superlattice structure using dedicated intra- and inter-layer force fields. The relaxed geometry suggested that ~10 nm away from the domain wall and beyond, the stacking is perfect with zero inter-layer twists or strain, in agreement with experiment. The topological number of domain walls that end at domain wall crossings is directly related to the global twist angle in a given section by dividing the number of domain walls within the section and can be obtained by the number of interatomic spacings along the section side. For example, the scale bar in figure 1a is 0.5 μm long (~ 2,500 interatomic spacings), and it crosses ten domain walls (a total shear of 10 interatomic spacings), indicating an angle of 10/2,500 radians.

d. 2D polarization calculation

The 2D polarization per interface is extracted directly from the measured ΔV_{KP} of a single active interface via the relation $P_{2D} = \frac{\epsilon_0 \Delta V_{\mathrm{KP}}}{2}$. With $\epsilon_0 = 8.854 \times 10^{-12}$ Fm^{-1} and $\Delta V_{\mathrm{KP}} \approx 120$ mV, we get $P_{\mathrm{2D}} \approx 0.53$ pCm^{-1}. This result is in agreement with the calculated value of $P_{2D} = \int_{-\infty}^{\infty} \rho_0^{ex}(z) z dz$, with $\rho_0^{ex}(z)$ being represented by the dashed black line in Fig. 4a,b.

e. Cumulative polarization magnitude

It is beneficial, perhaps, to consider a local potential switching by ~ 1 Volt in a device context. According to our MoS_2 measurements in Fig. 2f this requires ten layers (6.6 nm thick) with nine interfaces that switch from a $9_{\downarrow}$ (-0.5V) to a $9_{\uparrow}$ (+0.5V) configurations. For *h*-BN with its twice larger polarization per layer, only five layers are required, which are 1.75 nm thick only. We further note the large band gap for *h*-BN (~5 eV) that should extend potential saturation to larger values and prevent the screening of the switching electric field in stacks with more layers.

S2. Finite Ferroelectric-like coupling of two active interfaces

While the internal electric fields are mostly confined to the interfacial volume, as discussed in the main text, we find indications of finite coupling between adjacent regions of two active interfaces structures. This is achieved by comparing the average area coverage of co-aligned (ABC/CBA) and anti-aligned (ABA) domains (see Fig. S1e,f). The higher adhesion phase naturally expands on the expense of other stacking configurations[5]. Indeed, we find that regions in the map of large area domains (marked in black or green) show a clear preference for ABC or CBA stackings with ↑↑ or ↓↓ (bright or dark) polarization, respectively, at the expense of the anti-aligned ABA and BAB domains (with neutral-color) of ↑↓ or ↓↑ polarization, respectively. A close look at two active interface regions with smaller domains (outside the marks) also shows a reduced area of the neutral domains even away from the physical edge of the layers (although the area difference here is minor). Recently, we reported a similar behavior in a single active interface system of parallel *h*-BN bilayers, where domain wall sliding in response to an externally applied electric field promoted larger domains that align with the external field at the expense of the anti-aligned configuration[6] (see also Fig. 3a-c). As previously discussed,[6] the dynamics of this phenomenon is governed by the loss of adhesion energy in the domain wall network and the pinning from the disorder at the interface. The internal out-of-plane coupling reported here (with no external field) reveals a more stable ferroelectric coupling (ABCABC…) in comparison to the antiferroelectric order in the Bernal (ABAB..) configuration.

S3. Doping and de-polarization measurements

A precise measurement of the out-of-plane polarization at the high doping limit is challenging due to the KPFM signal sensitivity to long-range coulomb forces. The latter interacts with the tip's cantilever and cone rather than its local apex only[7]. While the side-band measurement mode overcomes this challenge to provide quantitative information at zero gate bias, its reliability drops as the external potential on the gate electrode and, correspondingly, the doping charge density on the TMD increase. Crucially, this measurement limitation can only underestimate (by averaging out) the local potential drop, ΔV_{KP}, between domains and its corresponding polarization magnitude. To minimize this underestimation, we used two complementary gating schemes, where either the sample potential is grounded and the gold electrode is biased or vice versa (Fig. S1b, a respectively). Data shown in the main text and in SI are recorded in the configuration of Fig. S1a.

We also focused on domains located next to the electrode's edges (while placing the cantilever outside them) and controlled the potential on the global silicon substrate independently. Additional limitations arise from the motion of domain walls at high charge doping and displacement fields, surface chemical adsorption, and surface degradation (see Fig. S2a-c). The latter hinders our quantitative analysis even with a very thin gate dielectric (down to 5 nm thick), where the maximum doping level (at the *h*-BN breakdown electric field) is reached at moderate gate potentials.

Lastly, localized defect states at the host crystals may reduce the occupation of delocalized states by the gate bias. This may result in some overestimation of the precise doping if extracted from the geometric capacitance only. To eliminate this overestimation, we extracted the doping density in Fig. 3d from the change in the average potential (V_{avg}), measured on oppositely polarized domains (as marked in Fig. 1b), rather than directly from the applied V_g. V_{avg} grows with V_g beyond some threshold value, and in one direction only for each particular sample (Fig. S2d). We attribute this behavior to unpinning of the Fermi-level from gap states associated with native dopants in each sample. The latter seems to prevent achieving electron and hole doping in the same sample. Importantly, V_{avg} is only sensitive to the mobile charge density that accumulates to screen the bottom electrode, regardless of internal properties of the electrodes such as localized defect states, Schottky barriers, or quantum capacitance. The deviation from the ideal $V_{avg} = -V_g$ (dashed black) slope at high $|V_{avg}|$ is attributed to the underestimation of the local KPFM signal in case of large doping levels and spatially alternating potentials at the edges of the electrodes, as discussed above. Altogether, the measurements in Fig. 3d provide an underestimation of the polarization magnitude and the mobile charge density.

We note that the present setup, which is dedicated for doping experiments is not ideal for studying reversible switching. The TMD structure is galvanically connected to one of the electrodes, thus a sensitive imaging of the system's response is limited to displacement fields of one polarity, quickly reaching a contrast plateau when reversing the polarity. To study the switching dynamics, it is beneficial to implement two external electrodes where opposite displacement fields can be switched effectively while probing the system response by other means (such as transport or electron beam imaging) [6,8–15]. This however hinders a direct measurement of doping effects on polarization.

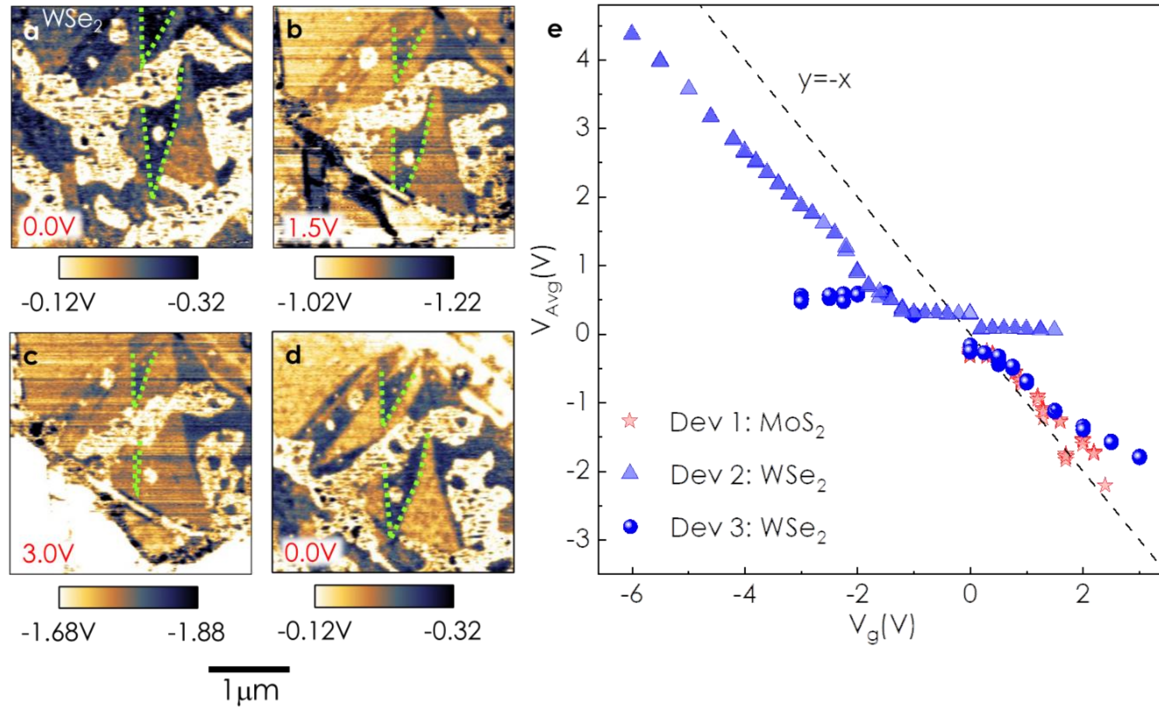

Figure S2. Doping and depolarization measurements. (a-d) Examples of surface potential maps obtained from a parallelly stacked WSe_2 bilayer under several gate biases V_g (Device 3). Note the domain wall motion at high doping density (dashed green lines) that extends bright areas over dark domains[6]. The panels demonstrate a reversible domain motion with applied gate bias from 0 V→1.5 V→3.0 V→-3 V (not shown) → 0 V. **(e)** The average KP potential of the TMD bilayers, V_{avg}, as a function of the applied gate potential, V_g.

S4. Calculation of multi-layered WSe_2 and MoS_2 polarization

In Figs. 1c and 2f of the main text we present the electrostatic potential profile along the normal direction of an ABC stacked WSe_2 trilayer and the thickness dependence of the polarization of parallelly stacked MoS_2 multilayered systems, respectively. The potential profiles were calculated using the Perdew-Burke-Ernzerhof (PBE) generalized-gradient exchange-correlation density functional approximation,[16] augmented by the Grimme-D3 dispersion correction with Becke-Johnson (BJ) damping[17] as implemented in the Vienna Ab-initio Simulation Package (VASP).[18] The core electrons of the Mo, W, S, and Se atoms were treated via the projector augmented wave (PAW) approach. Spin-orbit interactions were included. This level of theory was recently successfully used to calculate the polarization of transition metal dichalcogenide (TMD) bilayers.[12]

AB stacked WSe_2 and MoS_2 bilayers, constructed from two relaxed monolayers, were allowed to further relax, yielding lattice constants of 3.29 Å and 3.15 Å, respectively, and interlayer distances (defined as the normal distance between adjacent Se or S ions of the two layers) of 3.10 Å and 2.90 Å, respectively. Single-point electron density calculations were then performed on the relaxed structure with a plane wave energy cutoff of 600 eV and a k-point mesh of $12 \times 12 \times 1$, setting a vertical vacuum size of 10 nm to avoid interactions between adjacent bilayer images. To evaluate the vertical polarization, a dipole moment correction was employed. The potential and charge density profiles along the vertical direction of the two bilayers are shown in Fig. S3. The resulting difference between the electrostatic potential values obtained far above the top and below the bottom surfaces of the WSe_2 and MoS_2 bilayers are 69 meV and 82 meV, respectively, defining the vertical polarization of the two systems. Multilayered MoS_2 systems were constructed on the basis of the AB stacked bilayer by adding additional layers in the AB stacking configuration. Following further optimization, single point potential profile calculations were performed as detailed above.

Convergence tests of the VASP calculations (see Fig. S4) with respect to the vacuum size, energy cut-off, and number of reciprocal space k-points indicate that our choice of parameters leads to WSe_2 (MoS_2) binding energies that are converged to within 0.006 (0.0001), 0.002 (0.01), and 0.007 (0.003) meV/atom, respectively. Correspondingly, the electrostatic potential difference converges to within 0.01 (0.5), 0.05 (0.001), and 0.04 (0.03) meV with respect to the vacuum size, energy cut-off, and number of reciprocal space k-points, respectively.

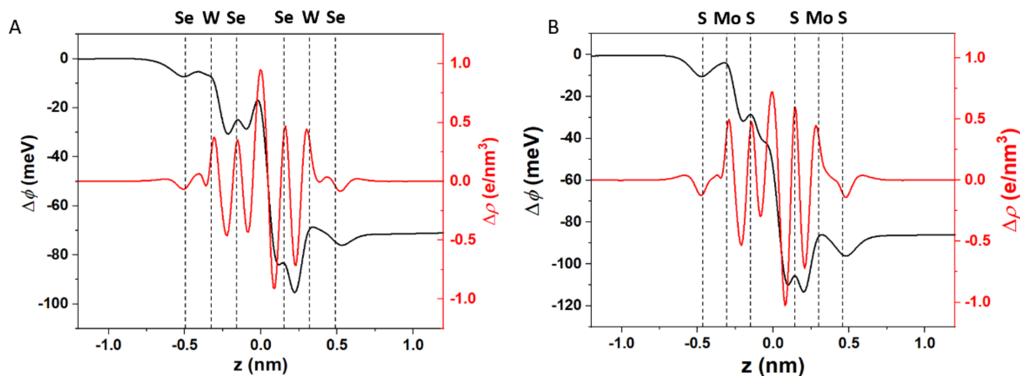

Figure S3. Potential and charge density profiles of WSe_2 and MoS_2 bilayers. Difference between bilayer and isolated monolayer plane-averaged potential (black) and charge density (red) for an AB stacked **(a)** WSe_2 and **(b)** MoS_2 bilayers. The dashed lines represent the vertical location of the ions. The origin of the horizontal axis is set to the midpoint between the layers.

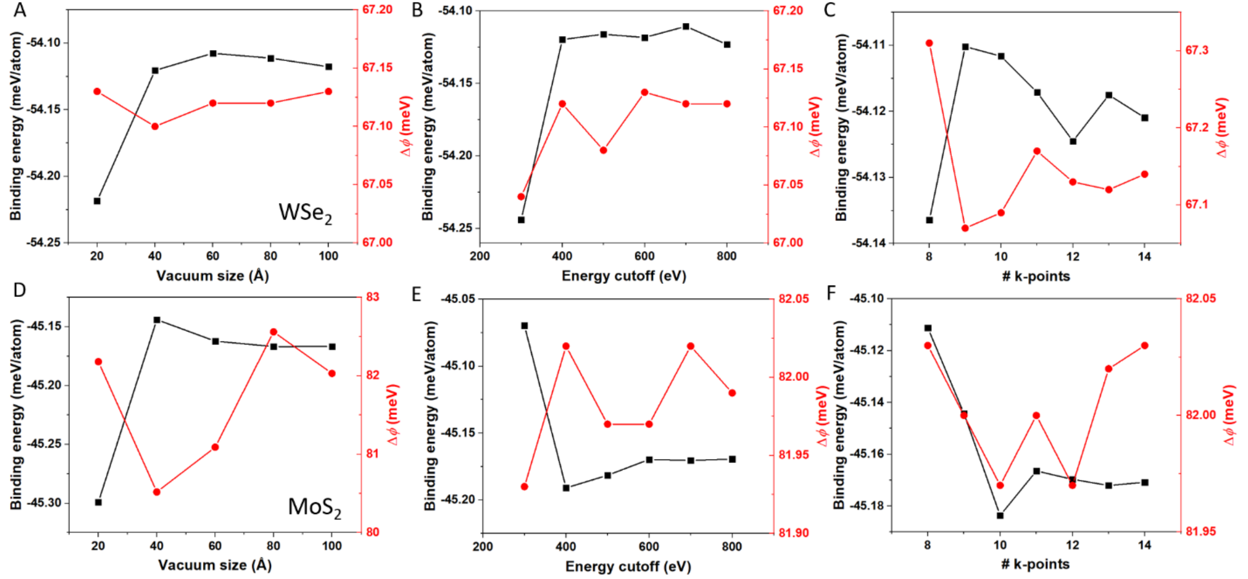

Figure S4. Convergence tests. Convergence tests of the binding energy (black curve, left vertical axis) and electrostatic potential difference (red curve, right vertical axis) of WSe_2 (top panels) and MoS_2 (bottom panels) bilay,ers (same structures as in Fig. S3) as a function of: **(a,d)** vacuum size; **(b,e)** energy cutoff, and **(c,f)** number of k-points.

S5. Calculation of doping-induced depolarization in WSe_2 and MoS_2

Doping calculations of bilayer WSe_2 and MoS_2 were performed using the fractional nuclear charge pseudoatom approach[19], allowing for simulating doping densities in the experimentally relevant range. To this end, we use pseudopotentials (PPs) generated for atoms with fractional nuclear charge. These calculations were performed using the open source Quantum Espresso package [20], instead of VASP that was used in section S4, allowing us to construct appropriate PPs. We first generated Rappe-Rabe-Kaxiras-Joannopoulos (RRKJ)[21] PPs, including spin-orbit interactions, using the ld1.x program of the plane-wave pseudopotential Quantum Espresso package[20,22]. The nuclear charge of the pseudoatom was set to the original charge of the neutral element plus a small fractional charge ε. For example, the nuclear charge of a doped pseudo W atom was set to $Z = 74 \pm \varepsilon$. The valence electronic charge was changed accordingly to maintain neutrality of the unit-cell, with an electron configuration given by [Xe]$4f^{14}6s^{2}6p^{0}5d^{4\pm\varepsilon}$. A set of PPs were generated by setting $\varepsilon = 10^{-9}, 10^{-8}, \dots, 10^{-2}$ for all W atoms in the bilayer system, corresponding to doping densities of $\Delta n_{2D} = 2.1 \times 10^{7}, 2.1 \times 10^{8}, \dots, 2.1 \times 10^{13}$ cm^{-2}, respectively. A similar procedure

was used to generate MoS_2 PPs with fractional nuclear charge and valence charge. For example, for a pseudo Mo nuclear charge of $Z = 42 \pm \varepsilon$, the electron configuration was set to $[\mathrm{Kr}]5s^2 5p^0 4d^{4\pm\varepsilon}$.

Single point calculations were performed using the generated PPs to obtain the electron density and the corresponding electrostatic potential profiles. To this end, we employed the PBE generalized-gradient density functional approximation[16] and the Grimme-D3 dispersion correction with BJ damping,[17] as implemented in Quantum Espresso. A plane wave energy cutoff of 60 Ry (816.34 eV) was used with a k-mesh of $12 \times 12 \times 1$, and a vertical vacuum size of 10 nm was set to avoid interactions between adjacent bilayer images. Fermi-Dirac smearing was used to enhance the convergence of the self-consistent cycle. To obtain the electrostatic potential profiles, a dipole moment correction was used.

As in the procedure discussed in section S4, AB-stacked WSe_2 and MoS_2 bilayers were first constructed and optimized, yielding lattice constants of 3.29 Å and 3.16 Å and interlayer distances of 3.05 Å and 2.95 Å, respectively. The resulting electrostatic potential drops were 71 meV and 76 meV for the undoped WSe_2 and MoS_2 bilayers, respectively. Note that little difference (2 and 6 meV for WSe_2 and MoS_2, respectively) was found between the potential drops calculated by VASP in section S4 and those obtained using Quantum Espresso. The potential and charge density profiles along the vertical direction for the two bilayers are shown in Fig. S5.

Convergence tests for the Quantum Espresso calculations (see Fig. S6) with respect to the vacuum size, energy cut-off, and number of k-points indicate that our choice of parameters leads to WSe_2 (MoS_2) binding energies that are converged to within 0.0003 (0.0003), 0.004 (0.003), and 0.003 (0.0004) meV/atom, respectively. Correspondingly, the electrostatic potential difference converges to within 2.6 (0.9), 3.8 (1.1), and 3.6 (2.4) meV with respect to the vacuum size, energy cut-off, and number of reciprocal space k-points, respectively.

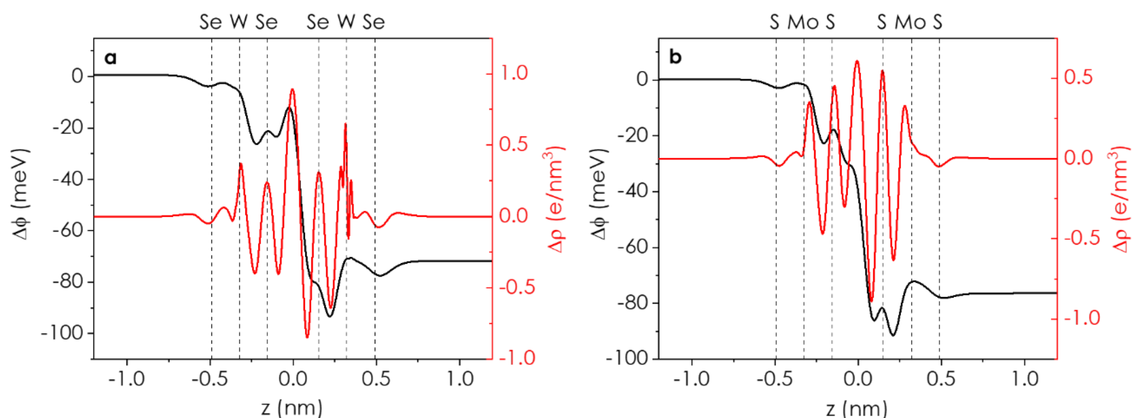

Figure S5. Potential and charge density profiles for WSe_2 and MoS_2 bilayer. Difference between bilayer and isolated monolayer plane-averaged potential (black) and charge density (red) for AB stacked **(a)** WSe_2 and **(b)** MoS_2 bilayers. The dashed lines represent the vertical location of the ions. The origin of the horizontal axis is set to the midpoint between the layers.

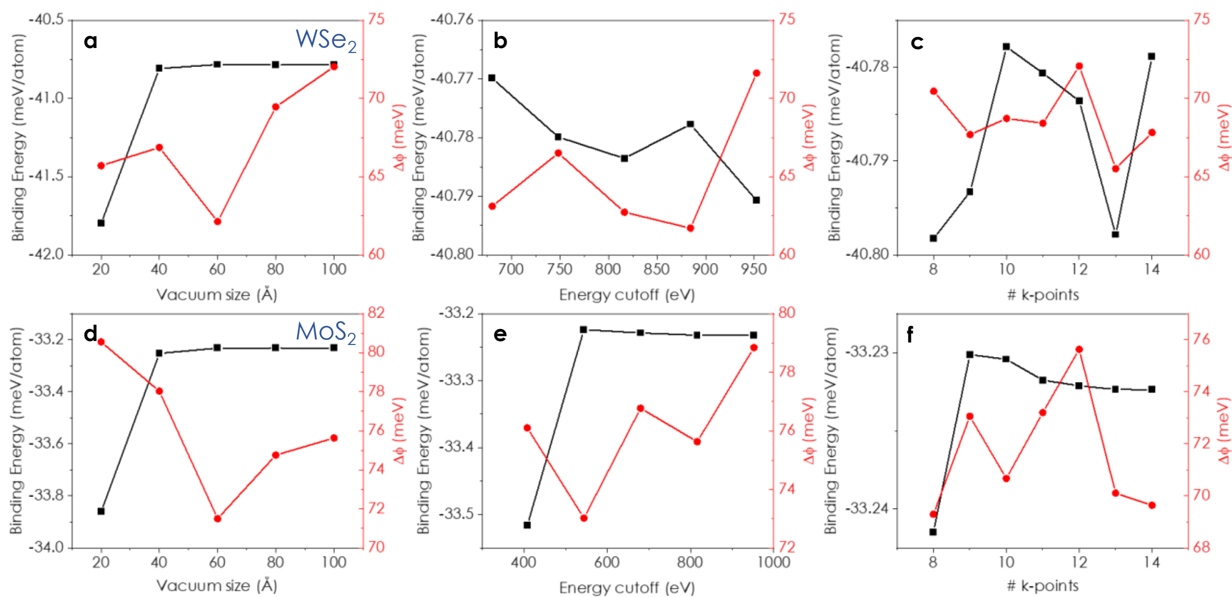

Figure S6. Convergence tests. Convergence tests of the binding energy (black curve, left vertical axis) and electrostatic potential difference (red curve, right vertical axis) of WSe_2 (top panels) and MoS_2 (bottom panels) bilayers (same structures as in Fig. S5) as a function of **(a, d)** vacuum size; **(b, e)** energy cutoff, and **(c,f)** number of k-points.

Doping of the WSe_2 and MoS_2 bilayers was performed by charging the metal nuclei. As discussed in the main text, up to a system dependent hole or electron charge density, the polarization remains mostly unaffected, following which a polarization drop is clearly seen (see Fig. S7). We note that the fractional nuclear charge pseudoatom doping approach[21] adopted in this study remains valid as long as variations in the calculated band-structure, induced by the nuclear pseudo charging, are negligible. To confirm that our calculations satisfy this condition, we compare the bandstructures of the undoped and doped WSe_2 (Fig. S8a) and MoS_2 (Fig. S8d) bilayers up to the highest doping density considered. Our results clearly demonstrate merely minor deviations of the band-structures of the doped systems from those of the undoped counterparts. The energy difference between the topmost K and Γ valence band points for the doped and undoped systems is presented in Fig. S8b and S8e for WSe_2 and MoS_2, respectively. Larger energy differences at higher doping levels result from the depolarization shown in Fig. S7. As an additional validity test, the doping-induced WSe_2 and MoS_2 Fermi level shifts are presented in Fig. S8c and S8f, respectively, exhibiting the expected logarithmic dependence[23] up to doping densities of 1×10^{13} cm^{-2}.

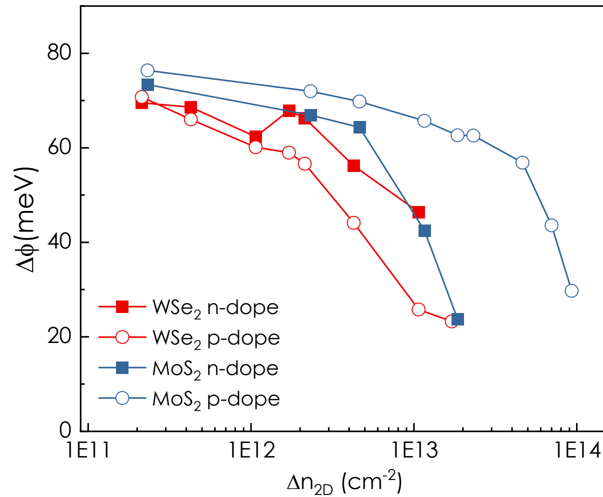

Figure S7. Effect of doping on the interlayer potential drop. The potential drop as a function of electron (*n*, filled squares) and hole (*p*, empty circles) doping density for AB stacked bilayer WSe_2 (red) and MoS_2 (blue). The doping is introduced via the metal pseudo nuclei.

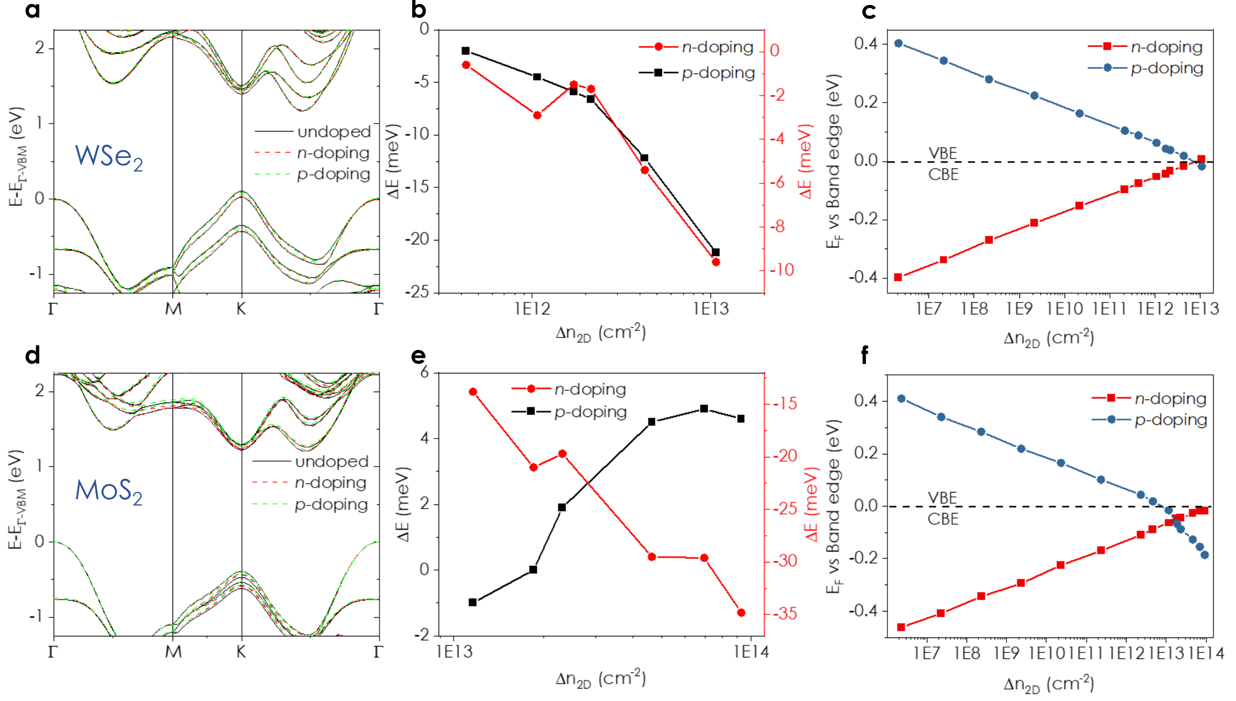

Figure S8. Band structure and Fermi level variations with doping charge density. (a, d) The band structures of undoped (black), *n*-doped (red), and *p*-doped (green) WSe_2 (a) and MoS_2 (d). For WSe_2 (MoS_2) the *n*-doped and *p*-doped band-structures are plotted for a charge density of $\Delta n_{2\mathrm{D}} = \mp 1.1 \times 10^{13}\ cm^{-2}$ ($\mp 9.3 \times 10^{13}\ cm^{-2}$), respectively. The origins of the vertical axes are set to the topmost Γ-point valence band energy ($\mathrm{E}_{\Gamma-\mathrm{VBM}}$). **(b, e)** The variation of the difference between the topmost K and Γ valence band energies as a function of doping density for (b) WSe_2 and (e) MoS_2. Results are presented with respect to the energy difference obtained for the undoped system: $\Delta E = [\mathrm{E}_{\mathrm{K-VBM}} - \mathrm{E}_{\Gamma-\mathrm{VBM}}]_{doped} - [\mathrm{E}_{\mathrm{K-VBM}} - \mathrm{E}_{\Gamma-\mathrm{VBM}}]_{undoped}$. **(c, f)** The Fermi level position of (c) WSe_2 and (f) MoS_2 as a function of *n*-doping (red) and *p*-doping (blue) charge densities. The origins of vertical axes are set to the conduction band minimum energy for *n*-doping and the valence band maximum energy for *p*-doping. The doping is introduced via the metal pseudo nuclei.

To demonstrate that our conclusions are independent on the choice of doping only via the metal atoms, we repeated the calculations by doping only via the chalcogen nuclei or doping all nuclei (see Fig. S9). Consistent results are obtained regardless of the doping scheme.

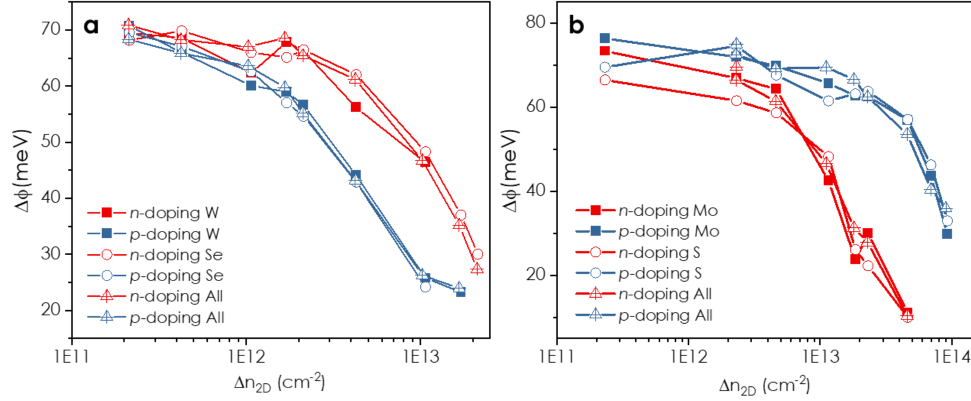

Figure S9. Comparison of different doping schemes. The polarization as a function of *n*-doping (red) and *p*-doping (blue) charge density for **(a)** WSe_2 and **(b)** MoS_2. Different doping schemes are applied including: only metal ions (filled squares), only chalcogen ions (open circles), or all ion doping (open triangle). For WSe_2, the W ion doping charge excess values were $\varepsilon = 10^{-4}, 2\times10^{-4}, 5\times10^{-4}, 8\times10^{-4}, 10^{-3}, 2\times10^{-3}, 5\times10^{-3}, 8\times10^{-3}, 0.01$; the Se ion doping charge excess values were $\varepsilon = 5\times10^{-5}, 10^{-4}, 2.5\times10^{-4}, 4\times10^{-4}, 5\times10^{-4}, 10^{-3}, 2.5\times10^{-3}, 4\times10^{-3}, 0.005$; and the all ion doping charge excess values used were $\varepsilon = 3.3\times10^{-5}, 6.6\times10^{-5}, 1.6\times10^{-4}, 2.6\times10^{-4}, 3.3\times10^{-4}, 6.6\times10^{-4}, 1.6\times10^{-3}, 2.6\times10^{-3}, 0.0033$. The electron configuration of Se was given by $[\mathrm{Ar}]3d^{10}4s^2 4p^{4\pm\varepsilon}$, and the corresponding nuclear charge was $Z = 34 \pm \varepsilon$. For MoS_2, the Mo ion doping charge excess values were $\varepsilon = 10^{-4}, 10^{-3}, 2\times10^{-3}, 5\times10^{-3}, 8\times10^{-3}, 0.01, 0.02, 0.03, 0.04$; the S ion doping charge excess values were $\varepsilon = 5\times10^{-5}, 5\times10^{-4}, 10^{-3}, 2.5\times10^{-3}, 4\times10^{-4}, 0.005, 0.01, 0.015, 0.02$; and the all ion doping charge excess values used were $\varepsilon = 3.3\times10^{-5}, 3.3\times10^{-4}, 6.6\times10^{-4}, 1.6\times10^{-3}, 2.6\times10^{-3}, 3.3\times10^{-3}, 6.6\times10^{-3}, 0.01, 0.013$. The electron configuration of S was given by $[\mathrm{Ne}]3s^2 3p^{4\pm\varepsilon}$, and the corresponding nuclear charge was $Z = 16 \pm \varepsilon$.

S6. Effect of polarization on the band-structure

To evaluate the effect of the emerging polarization on the band structure, we compare in Fig. S10 the band structure of the anti-parallel AA' stacked undoped bilayers with those of the parallel AB stacked counterparts, all evaluated at the same level of theory as described in section S5. The results clearly demonstrate band splitting of both the conduction and the valence bands at the K point. Notably, this splitting is of the order of the calculated vertical potential drops (see SI section S5 above), indicating that the emerging polarization is indeed causing the splitting.

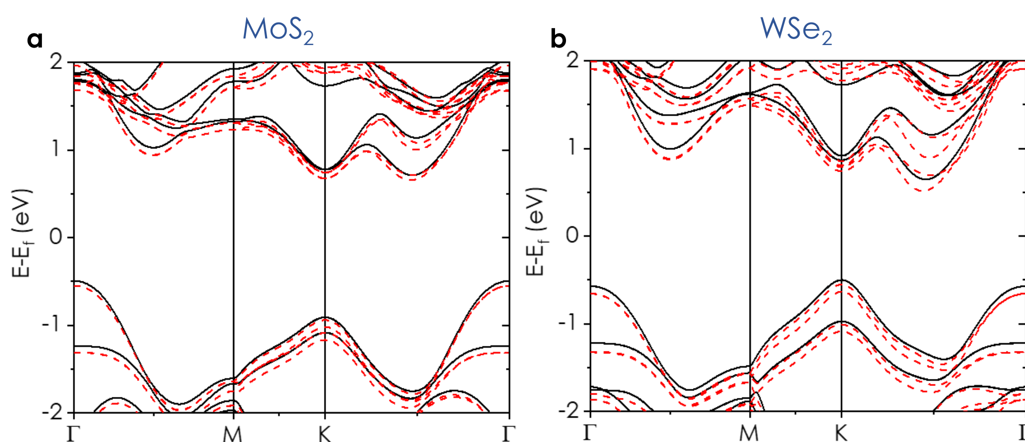

Figure S10. Effect of polarization on the band structure. The band structures of **(a)** MoS_2 and **(b)** WSe_2 bilayers at their anti-parallel AA' (solid black curve) and parallel AB (dashed red curve) stacking modes.

References:

1. Panchal, V., Pearce, R., Yakimova, R., Tzalenchuk, A. & Kazakova, O. Standardization of surface potential measurements of graphene domains. *Sci. Rep.* **3**, 2597 (2013).

2. Liscio, A., Palermo, V. & Samorì, P. Nanoscale quantitative measurement of the potential of charged nanostructures by electrostatic and Kelvin probe force microscopy: Unraveling electronic processes in complex materials. *Acc. Chem. Res.* **43**, 541–550 (2010).

3. Melios, C. *et al.* Carrier type inversion in quasi-free standing graphene: Studies of local electronic and structural properties. *Sci. Rep.* **5**, 10505 (2015).

4. Alden, J. S. *et al.* Strain solitons and topological defects in bilayer graphene. *Proc. Natl. Acad. Sci. U. S. A.* **110**, 11256–11260 (2013).

5. Weston, A. *et al.* Atomic reconstruction in twisted bilayers of transition metal dichalcogenides. *Nat. Nanotechnol.* **15**, 592–597 (2020).

6. Vizner Stern, M. *et al.* Interfacial ferroelectricity by van der Waals sliding. *Science (80-.).* **372**, 142–1466 (2021).

7. Collins, L., Kilpatrick, J. I., Kalinin, S. V. & Rodriguez, B. J. Towards nanoscale electrical measurements in liquid by advanced KPFM techniques: a review. *Reports Prog. Phys.* **81**, 086101 (2018).

8. Fei, Z. *et al.* Ferroelectric switching of a two-dimensional metal. *Nature* **560**, 336–339 (2018).

9. Yuan, S. *et al.* Room-temperature ferroelectricity in MoTe2 down to the atomic monolayer limit. *Nat. Commun. 2019 101* **10**, 1–6 (2019).

10. Sharma, P. *et al.* A room-temperature ferroelectric semimetal. *Sci. Adv.* **5**, (2019).

11. de la Barrera, S. C. *et al.* Direct measurement of ferroelectric polarization in a tunable semimetal. *Nat. Commun. 2021 121* **12**, 1–9 (2021).

12. Wang, X. *et al.* Interfacial ferroelectricity in rhombohedral-stacked bilayer transition metal dichalcogenides. *Nat. Nanotechnol.* (2022) doi:10.1038/s41565-021-01059-z.

13. Wan, Y. *et al.* Room-Temperature Ferroelectricity in 1 T ′ - ReS 2 Multilayers . *Phys. Rev. Lett.* **128**, 067601 (2022).

14. Weston, A. *et al.* Interfacial ferroelectricity in marginally twisted 2D semiconductors. *Nat. Nanotechnol.* **17**, 390–395 (2022).

15. Lipatov, A. *et al.* Direct observation of ferroelectricity in two-dimensional MoS2. *npj 2D Mater. Appl.* **6**, 18 (2022).

16. Perdew, J. P., Burke, K. & Ernzerhof, M. Generalized gradient approximation made simple. *Phys. Rev. Lett.* **77**, 3865–3868 (1996).

17. Grimme, S., Antony, J., Ehrlich, S. & Krieg, H. A consistent and accurate ab initio parametrization of density functional dispersion correction (DFT-D) for the 94 elements H-Pu. *J. Chem. Phys.* **132**, 154104 (2010).

18. Kresse, G. & Furthmüller, J. Efficient iterative schemes for ab initio total-energy calculations using a plane-wave basis set. *Phys. Rev. B - Condens. Matter Mater. Phys.* **54**, 11169–11186 (1996).

19. Sinai, O. & Kronik, L. Simulated doping of Si from first principles using pseudoatoms. *Phys. Rev. B - Condens. Matter Mater. Phys.* **87**, 235305 (2013).

20. Giannozzi, P. *et al.* QUANTUM ESPRESSO: a modular and open-source software project for quantumsimulations of materials. *J. Phys. Condens. Matter* **21**, 395502 (2009).

21. Rappe, A. M., Rabe, K. M., Kaxiras, E. & Joannopoulos, J. D. Optimized pseudopotentials. *Phys. Rev. B* **41**, 15 (1990).

22. Dal Corso, A. Pseudopotentials periodic table: From H to Pu. *Comput. Mater. Sci.* **95**, 337–350 (2014).

23. Colinge, J. P. & Colinge, C. A. *Physics of Semiconductor Devices*. (Kluwer Academic Publishers, 2002). doi:10.1007/b117561.